
DNOI-4DRO: Deep 4D Radar Odometry with Differentiable Neural-Optimization Iterations

Shouyi Lu

Tongji University

School of Automotive Studies

2210803@tongji.edu.cn

Huanyu Zhou

Tongji University

School of Automotive Studies

2231634@tongji.edu.cn

Guirong Zhuo

Tongji University

School of Automotive Studies

zhuoguirong@tongji.edu.cn

Abstract

A novel learning-optimization-combined 4D radar odometry model, named DNOI-4DRO, is proposed in this paper. The proposed model seamlessly integrates traditional geometric optimization with end-to-end neural network training, leveraging an innovative differentiable neural-optimization iteration operator. In this framework, point-wise motion flow is first estimated using a neural network, followed by the construction of a cost function based on the relationship between point motion and pose in 3D space. The radar pose is then refined using Gauss-Newton updates. Additionally, we design a dual-stream 4D radar backbone that integrates multi-scale geometric features and clustering-based class-aware features to enhance the representation of sparse 4D radar point clouds. Extensive experiments on the VoD and Snail-Radar datasets demonstrate the superior performance of our model, which outperforms recent classical and learning-based approaches. Notably, our method even achieves results comparable to A-LOAM with mapping optimization using LiDAR point clouds as input. Our models and code will be publicly released.

1 Introduction

Odometry is critical to autonomous driving systems, particularly in GPS-denied environments. It involves using consecutive images or point clouds to estimate the relative pose transformation between two frames. Most existing odometry methods focus primarily on 2D visual odometry [1, 2, 3, 4, 5] or 3D LiDAR [6, 7, 8, 9, 10, 11, 12]. However, the inherent characteristics of cameras and LiDARs make these methods vulnerable to challenging weather conditions such as rain, snow, or fog, compromising their robustness in these scenarios.

4D millimeter-wave radar, as an emerging automotive sensor, presents distinct advantages, including robustness under challenging weather and illumination conditions, the ability to measure object velocities and cost-effectiveness [13, 14, 15, 16, 17, 18]. These advantages have driven extensive research into 4D Radar Odometry (4DRO). Previous 4D radar odometry works can be classified into two categories: classical methods [19, 20, 21] and learning-based methods [22, 23]. Classical 4DRO systems typically consist of point cloud association and nonlinear optimization. Nonlinear optimization is critical in enhancing accuracy by integrating continuous sensor observations to optimize long-range trajectories. However, these methods have limited robustness because of the extracted features' poor quality and low resolution [19, 20]. With the development of deep learning, some methods [23, 24] attempt to utilize learning-based methods for 4D radar pose estimation. These

methods extract features from two point clouds using a feature extraction network, perform point cloud matching through a feature association network, and finally estimate the pose using a decoding network. Although this direct pose regression method, which does not rely on explicit optimization, can sometimes be more robust, its accuracy often shows limitations across various environments.

To address these problems, we propose DNOI-4DRO, a novel learning-optimization combined 4D radar odometry model. DNOI-4DRO integrates traditional geometric optimization into end-to-end neural network training through an innovatively designed differentiable neural-optimization iteration operator, leveraging the strengths of both classical methods and deep networks. Specifically, we estimate the point-wise motion flow using a neural network, construct the cost function based on the motion and pose relationships of points in 3D space, and update the radar pose using the Gauss-Newton to maximize its compatibility with the current point motion flow estimate. Furthermore, to extract robust 4D radar point features, we propose a novel feature extraction network that enhances the representation of radar point clouds by integrating multi-scale geometric features with clustering-based class-aware features, thereby improving motion estimation in complex environments. We perform extensive evaluation across two datasets, demonstrating state-of-the-art performance in all cases. To summarize, our main contributions are as follows:

(1) We propose DNOI-4DRO, a novel framework for 4D radar odometry. By exploiting the relationship between point motion and pose, DNOI-4DRO couples a geometric optimizer with a neural network to construct a fully end-to-end architecture. (2) We specially design an efficient radar feature extractor comprising a dual-stream 4D radar backbone, which extracts radar features with two representations and is further enhanced by a global Transformer. (3) Finally, our method is demonstrated on VoD [25] and Snail-Radar [26] datasets. Our method outperforms all classical and learning-based 4D radar odometry methods, achieving competitive results with A-LOAM, which uses LiDAR point clouds as input.

2 Related Work

2.1 Classical 4D Radar Odometry

Due to the similarity in spatial representation between 4D radar and LiDAR point clouds, most existing classical 4D radar odometry methods either directly adopt LiDAR odometry methods or modify them accordingly. Iterative Closest Point (ICP) is the most widely used LiDAR odometry method, computing relative pose transformations by minimizing the Euclidean distance between two point clouds. Based on error measurement, ICP can be categorized into ICP-point2point [27] and ICP-point2plane [28], aiming to shorten point-to-point and point-to-plane distances. Generalized ICP (GICP) [29] further intends to combine the advantages of both. Building on GICP, 4DRadarSLAM [19] models the spatial probabilistic distribution of radar points based on uncertainties in range and azimuth angle measurements. It proposes an Adaptive Probability Distribution-GICP (APDGICP) method based on the modeling results. RIV-SLAM [30] further refines this by considering the impact of the angle of arrival on radar measurement uncertainty to achieve a more accurate spatial probabilistic distribution of radar points. In addition to ICP, the Normal Distribution Transform (NDT) [31] is a widely used LiDAR odometry method. NDT represents point clouds with Gaussian distributions, converting pose estimation into an optimization problem that minimizes the Gaussian distribution error between the source and target point clouds. Expanding upon NDT, Li et al. [20] integrate the measurement uncertainties of 4D radar points into the calculations for the mean and variance of the normal distribution, aiming to reduce degradation effects caused by sparse 4D radar point clouds. Additionally, 4D iRIOM [32] introduces a point cloud registration method based on a distribution-to-multi-distribution distance metric, effectively addressing the sparsity issue of 4D radar point clouds and enhancing pose estimation robustness.

Our method draws on the cost function modeling approach of the ICP-point2point [27], a simpler optimization problem that avoids extracting complex representations like line and plane features. Instead of relying on nearest-neighbor queries to find matching points, our method uses a neural network to estimate the point motion field. This approach mitigates the challenging non-bijective correspondence between two point clouds caused by the sparsity and noise inherent in 4D radar point clouds.

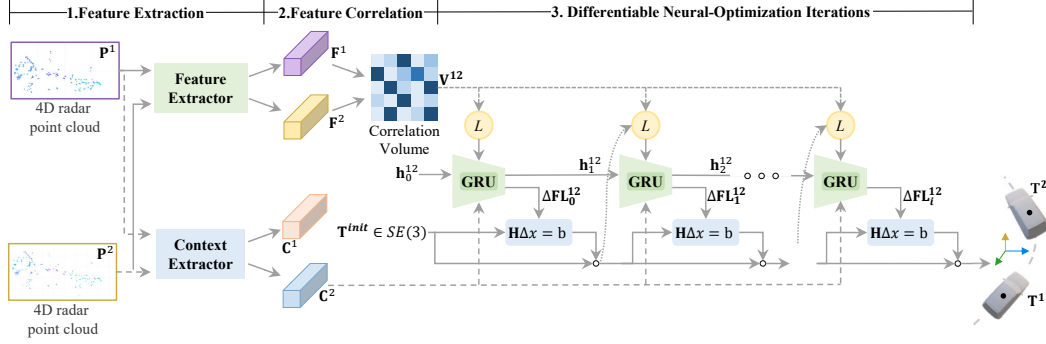


Figure 1: Overview of our backbone. (1) The feature and context extractors encode the point and context features of the input point cloud, respectively. (2) The feature correlation module constructs an all-pair correlation volume by calculating the matrix dot product of two-point features. (3) In each iteration, the differentiable neural-optimization iteration operator uses the pose estimated in the previous iteration to look up correlation features from the correlation volume, which are then processed through a GRU [37] to generate a point motion field. The point motion field is fed into a least-squares-based optimization layer, where the pose is updated based on geometric constraints. After multiple iterations, the network outputs the predicted pose.

2.2 Deep 4D Radar Odometry

Deep learning has made significant strides in visual and LiDAR odometry, yet 4D radar odometry remains a challenging problem. 4DRONet [23] proposes a sliding-window-based hierarchical optimization method to estimate and refine poses in a coarse-to-fine manner. SelfFRO [33] introduces a self-supervised 4D radar odometry method that uses radar point velocity information to construct a novel velocity-aware loss function, effectively guiding network training. CMFFlow [34] introduces a cross-modal supervision approach for estimating 4D radar scene flow, simultaneously providing pose estimation as an intermediate output. CAO-RONet [24] introduces a sliding-window-based optimizer that leverages historical priors to enable coupled state estimation and correct inter-frame matching errors. Although these methods show promising results, they often suffer from limited accuracy across diverse environments, and their interpretability remains constrained.

Moreover, we are inspired by the “Differentiable Recurrent Optimization-Inspired Design” proposed by DROID-SLAM [1] for visual odometry. The work combines iterative visual correspondence updates with differentiable bundle adjustments to optimize pose estimation. This concept has also been applied to optimizing pixel-level 3D motion [35]. However, both works are based on RAFT [36], which performs optical flow updates and optimizes variables in 2D space. This paper applies the idea to 3D space and a neural-optimization iteration module specifically for 3D point cloud odometry is being built for the first time.

3 DNOI-4DRO

We propose a backbone network for pose estimation between two 4D radar point clouds and then construct a 4DRO system upon it. We provide an overview in Fig. 1. The backbone network firstly extracts robust point and context features for each 4D radar point cloud, as introduced in Sec. 3.1. Then, the feature correlation volume is constructed using point features, which will be described in Sec. 3.2. Next, the differentiable neural-optimization iteration operator is introduced in Sec. 3.3 for pose estimation and refinement. Finally, the network outputs the pose $\mathbf{T}^1 \in \mathbb{R}^{4 \times 4}$ and $\mathbf{T}^2 \in \mathbb{R}^{4 \times 4}$ of the two 4D radar point clouds in the world coordinate system.

3.1 Feature Extraction

We employ two radar feature extraction networks with identical architectures but distinct functions to extract the point and context features from the 4D radar point cloud. The context features are provided as input to the recurrent iteration operator, whereas the point features are used to evaluate the point similarity using a dot product. To obtain fine-grained 4D radar point features, we propose a dual-stream 4D radar encoding network that integrates multi-scale geometric feature extraction,

clustering-based class-aware feature extraction, and a global Transformer module, as illustrated in Fig. 2. This network offers a more comprehensive feature representation for each 4D radar point, thereby significantly improving the robustness of odometry across diverse environments.

3.1.1 Multi-scale Geometric Feature Extraction

Given the 4D radar point clouds $\mathbf{P} = \{\mathbf{p}_i | \mathbf{p}_i \in \mathbb{R}^3\}_{i=1}^N$, we employ four parallel Set Abstraction (SA) layers [38] to encode the multi-scale geometric features. Each SA layer uses a different grouping radius to address the issue of non-uniform density in radar point clouds. At each scale s , each radar point \mathbf{p}_i generates a local geometric feature $\mathbf{f}_{i,s}^{\text{geo}}$. The geometric features across all scales are concatenated to form the multi-scale geometric feature representation of the 4D radar point, $\mathbf{f}_i^{\text{geo}} = \text{concat}(\{\mathbf{f}_{i,s}^{\text{geo}}\}_{s=0}^3)$.

3.1.2 Clustering-based Class-aware Feature Extraction

Inspired by Context Clusters [39], which proposes a generic clustering-based visual backbone viewing images as a set of points, we extend it and propose a novel clustering-based class-aware 4D radar point feature extraction method, consisting primarily of three components: 4D radar point clustering, class-aware feature aggregation, and feature dispatching.

4D Radar Point Clustering: We first use PointNet [40] to map the 4D radar points to a high-dimensional feature space \mathbf{f}_i^p for similarity computation. Next, we apply Farthest Point Sampling (FPS) [38] to evenly select C center points in space, and the center feature \mathbf{f}_j^{ct} is computed by averaging its K nearest points. We then calculate the pairwise cosine similarity matrix $\mathbf{S} \in \mathbb{R}^{C \times N}$ between each point and the set of center points. After that, we allocate each point to the most similar center, resulting in C clusters.

Class-aware Feature Aggregation: Following [39], we dynamically aggregate all radar point features within the same cluster based on the similarities to the cluster center. Given the cluster which contains M radar points around the j -th cluster center, the aggregated feature \mathbf{f}_j^a is calculated by:

$$\mathbf{f}_j^a = \frac{1}{\mathbf{A}} \left(\mathbf{f}_j^{\text{ct}} + \sum_{m=1}^M \text{sigmoid}(\alpha s_{jm} + \beta) \cdot \mathbf{f}_m^p \right), \quad \mathbf{A} = 1 + \sum_{m=1}^M \text{sigmoid}(\alpha s_{jm} + \beta), \quad (1)$$

where \mathbf{f}_j^{ct} represents the feature of the j -th cluster center, and s_{jm} denotes the similarity score between the m -th radar point and the j -th cluster center. α and β are learnable scalars used to scale and shift the similarity, while $\text{sigmoid}(\cdot)$ is the sigmoid function that rescales the similarity to (0,1). \mathbf{A} is the normalization factor.

Feature Dispatching: After obtaining the class-aware aggregated features, we employ an adaptive process to assign each point within a cluster based on its similarity, resulting in a more coherent and representative understanding of the overall structure and context within the cluster. For each point embedding \mathbf{f}_m^p , the updated point embedding \mathbf{f}_m^c is computed using the following formula:

$$\mathbf{f}_m^c = \mathbf{f}_m^p + \text{sigmoid}(\alpha s_{jm} + \beta) \cdot \mathbf{f}_j^a, \quad (2)$$

We concatenate the multi-scale geometric features of radar points with the class-aware features to construct the geometric-class joint feature representation \mathbf{f}_i^l .

3.1.3 Global Transformer

The global transformer employs an attention mechanism [41] across the entire radar point cloud to capture the long-range correlation of points. For each point $\mathbf{p}_i \in \mathbf{P}$, the global transformer applies an attention mechanism to all other points $\mathbf{p}_j \in \mathbf{P}$:

$$\mathbf{f}_i = \sum_{\mathbf{f}_j^l \in \mathcal{X}^l} \langle \alpha^g(\mathbf{f}_i^l), \beta^g(\mathbf{f}_j^l) \rangle \gamma^l(\mathbf{f}_j^l), \quad (3)$$

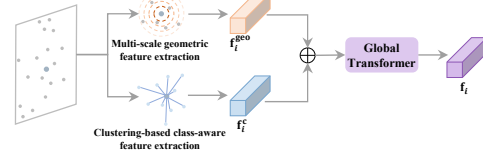


Figure 2: The structure of dual-stream radar feature extraction network.

where \mathcal{X}^1 represents the geometric-class joint feature set, $\alpha^g(\cdot)$, $\beta^g(\cdot)$, and $\gamma^g(\cdot)$ are shared learnable linear transformations. $\langle \cdot \rangle$ denotes a scalar product. Linear layer, layer norm, and skip connection are further applied to complete the global transformer module.

3.2 Feature Correlation

We construct a feature correlation volume by evaluating feature similarity between all point pairs. Given point features $\mathbf{F}^1 = \{\mathbf{f}_i^1 | \mathbf{f}_i^1 \in \mathbb{R}^D\}_{i=1}^N$ and $\mathbf{F}^2 = \{\mathbf{f}_j^2 | \mathbf{f}_j^2 \in \mathbb{R}^D\}_{j=1}^N$, where D is the feature dimension, the correlation volume $\mathbf{V}^{12} \in \mathbb{R}^{N \times N}$ can be computed through matrix dot product:

$$\mathbf{V}^{12} = \mathbf{F}^1 \cdot (\mathbf{F}^2)^T. \quad (4)$$

3.3 Differentiable Neural-Optimization Iteration Operator

The core of our approach is the differentiable neural-optimization iteration operator, which contains three key parts, as illustrated in Fig. 3: (1) an adaptive patch-to-patch correlation lookup method that retrieves correlation features from the precomputed correlation volume; (2) a GRU [37] that predicts updates to the point motion flow along with associated confidence weights; and (3) an All-point Motion-only Bundle Adjustment layer (AMBA) computes pose that aligns with the newly predicted point motion flow and confidence.

3.3.1 Adaptive Patch-to-Patch Correlation Look-up Layer

At the start of each iteration, we use the pose estimates from the previous iteration to calculate the correspondences. Specifically, for the i -th iteration, given the point clouds \mathbf{P}^1 and \mathbf{P}^2 , along with their respective poses \mathbf{T}_i^1 and \mathbf{T}_i^2 , we compute the all-point correspondence field $\mathbf{P}_i^{12} \in \mathbb{R}^{N \times 3}$:

$$\mathbf{P}_i^{12} = \mathbf{T}_i^{12} \cdot \mathbf{P}^1, \quad \mathbf{T}_i^{12} = \mathbf{T}_i^2 \cdot (\mathbf{T}_i^1)^{-1}, \quad (5)$$

\mathbf{P}_i^{12} represents the coordinates of points \mathbf{P}^1 mapped into \mathbf{P}^2 using the estimated pose. Then, we incorporate the Patch-to-Patch correlation concept from HALFlow [42] into the point correlation look-up mechanism of PV-RAFT [43] to learn fine-grained correlation features of sparse 4D radar points, thereby guiding the right flowing direction of point motion. Specifically, for each point $\mathbf{p}_{i,j}^{12}$ in \mathbf{P}_i^{12} , we first retrieve the initial correlation features from the correlation volume using nearest neighbor queries. Subsequently, based on the 3D local geometric structure of $\mathbf{p}_{i,j}^{12}$ and its neighboring points in \mathbf{P}_i^{12} , we adaptively weight the initial correlation features of these neighbors to obtain the final correlation feature $\mathbf{cf}_{i,j}^{12}$.

3.3.2 Point Motion Flow Update and Confidence Weight Prediction

We encode motion features using the correlation features $\mathbf{CF}_i^{12} = \{\mathbf{cf}_{i,j}^{12} | \mathbf{cf}_{i,j}^{12} \in \mathbb{R}^D\}_{j=1}^N$, the context features \mathbf{C}^1 , and the flow estimate $\mathbf{FL}_i^{12} \in \mathbb{R}^{N \times 3}$ from the previous iteration:

$$\mathbf{MF}_i^{12} = \text{concat}(\mathbf{CF}_i^{12}, \mathbf{C}^1, \text{MLP}(\mathbf{FL}_i^{12})). \quad (6)$$

The motion features \mathbf{MF}_i^{12} is used as the input to the GRU [37] to update the current hidden state \mathbf{h}_i^{12} . Instead of predicting updates to the pose directly, we predict updates in the space of point motion flow fields. We map the updated hidden state through two additional MLP layers to produce two outputs: (1) a revision flow field $\Delta\mathbf{FL}_i^{12} \in \mathbb{R}^{N \times 3}$ and (2) associated confidence $\mathbf{w}_i^{12} \in \mathbb{R}_+^{N \times 3}$. The revision $\Delta\mathbf{FL}_i^{12}$ is a correction term predicted by the network to correct errors in the all-point correspondence field. We denote the corrected correspondence as $\mathbf{P}_i^{12*} = \mathbf{P}_i^{12} + \Delta\mathbf{FL}_i^{12}$. The confidence term is further processed with a sigmoid operation to constrain its values within the $(0, 1)$. This term mitigates the adverse impact of inaccurate point motion flow estimation caused by occlusion, moving objects and noisy points on pose estimation accuracy.

3.3.3 All-point Motion-only Bundle Adjustment Layer

The All-point Motion-only Bundle Adjustment Layer (AMBA) maps flow revisions into pose updates. The primary objective of the AMBA layer is to minimize the discrepancy between the transformed point cloud and the corrected correspondence \mathbf{P}_i^{12*} . Specifically, we define the cost function as:

$$E(\mathbf{T}^1, \mathbf{T}^2) = \|r(\mathbf{T}^1, \mathbf{T}^2)\|_{\Sigma_{12}}^2 = \|\mathbf{P}_i^{12*} - \mathbf{T}^2 \cdot (\mathbf{T}^1)^{-1} \cdot \mathbf{P}^1\|_{\Sigma_{12}}^2, \quad (7)$$

where $\|\cdot\|_{\Sigma}^2$ is the Mahalanobis distance which weights the error terms based on the confidence weights \mathbf{w}_i^{12} . In this paper, we optimize the pose using the Gauss-Newton algorithm, based on the special Euclidean Lie algebra $\text{se}(3) = \left\{ \xi = \begin{pmatrix} \rho \\ \phi \end{pmatrix}, \rho \in \mathbb{R}^3, \phi \in \text{so}(3) \right\}$. First, we compute the Jacobian matrices $\mathbf{J}^1 \in \mathbb{R}^{N \times 3 \times 6}$ and $\mathbf{J}^2 \in \mathbb{R}^{N \times 3 \times 6}$ of the residual term $r(\mathbf{T}^1, \mathbf{T}^2)$ with respect to \mathbf{T}^1 and \mathbf{T}^2 using the perturbation model. For \mathbf{T}^2 , we apply the perturbation $\text{Exp}(\xi^2)$ on the left, which results in:

$$\mathbf{J}^2 = \frac{\partial r}{\partial \xi^2} = - \lim_{\xi^2 \rightarrow 0} \frac{\text{Exp}(\xi^2) \circ \mathbf{T}^{12} \circ \mathbf{P}^1 - \mathbf{T}^{12} \circ \mathbf{P}^1}{\xi^2} = - \begin{bmatrix} \mathbf{I} & -(\mathbf{R}^{12} \circ \mathbf{P}^1 + \mathbf{t}^{12})^{\wedge} \\ \mathbf{0}^T & \mathbf{0}^T \end{bmatrix}, \quad (8)$$

where $\text{Exp}(\cdot)$ represents the exponential map from Lie algebra to Lie group, and $(\cdot)^{\wedge}$ denotes the antisymmetric matrix operation. For \mathbf{T}^1 , we similarly apply the perturbation $\text{Exp}(\xi^1)$ and use the adjoint operator and chain rule of differentiation, which results in:

$$\begin{aligned} \mathbf{J}^1 &= \frac{\partial r}{\partial \xi^1} = - \lim_{\xi^1 \rightarrow 0} \frac{\text{Exp}(-\text{Adj}_{\mathbf{T}^{12}} \xi^1) \circ \mathbf{T}^{12} \circ \mathbf{P}^1 - \mathbf{T}^{12} \circ \mathbf{P}^1}{\xi^1} \\ &= \begin{bmatrix} \mathbf{I} & -(\mathbf{R}^{12} \circ \mathbf{P}^1 + \mathbf{t}^{12})^{\wedge} \\ \mathbf{0}^T & \mathbf{0}^T \end{bmatrix} \circ \text{Adj}_{\mathbf{T}^{12}}, \end{aligned} \quad (9)$$

where $\text{Adj}(\cdot)$ denotes the adjoint operator. We concatenate the Jacobian matrices \mathbf{J}^1 and \mathbf{J}^2 to obtain the Jacobian matrix $\mathbf{J} \in \mathbb{R}^{N \times 3 \times 12}$ of the residual term concerning the optimization variables.

Then, we linearizes the residual terms, and solves for the update:

$$\mathbf{J}^T \text{diag}(\mathbf{w}_i^{12}) \mathbf{J} \Delta \xi = -\mathbf{J}^T r(\mathbf{T}^1, \mathbf{T}^2), \quad (10)$$

where $\Delta \xi = (\Delta \xi^1, \Delta \xi^2)$ represents the pose update in the Lie algebra. Eqn.10 can be rewritten as a linear system:

$$\mathbf{H} \Delta \xi = \mathbf{b}, \quad \mathbf{H} = \mathbf{J}^T \text{diag}(\mathbf{w}_i^{12}) \mathbf{J}, \quad \mathbf{b} = -\mathbf{J}^T r(\mathbf{T}^1, \mathbf{T}^2). \quad (11)$$

This linear system is solved using Cholesky decomposition to obtain the updates $\Delta \xi^1$ and $\Delta \xi^2$. The updates refine the pose estimates from the previous iteration, and the updated poses serve as input for the next neural-optimization iteration module:

$$\mathbf{T}_{i+1}^1 = \text{Exp}(\Delta \xi^1) \cdot \mathbf{T}_i^1, \quad \mathbf{T}_{i+1}^2 = \text{Exp}(\Delta \xi^2) \cdot \mathbf{T}_i^2. \quad (12)$$

Based on the properties of the Jacobian matrix and Cholesky decomposition, gradients are backpropagated using the chain rule. Consequently, the AMBA layer functions as a differentiable optimization layer, enabling end-to-end training of the entire architecture during the training process.

4 Training and Implementation

DNOI-4DRO is implemented in PyTorch, with the LieTorch extension [44] used to perform back-propagation in the tangent space of all group elements.

4.1 Constructing Frame Graph

Each training example consists of a 7-frame 4D radar point cloud sequence. For each point cloud frame in the training samples, edges are constructed with its three nearest neighboring frames to form a frame graph. In this graph, any two frames connected by an edge undergo pose estimation using the backbone network. Additionally, to remove the 6-dof gauge freedom, the first pose in each training sample is fixed to the ground truth.

| Method | | | | | | | | | | | Mean | | | | | | |
|-------------------------|--------------------|--------------|--------------|--------------|--------------|--------------|--------------|--------------|--------------|--------------|--------------|--------------|--------------|--------------|--------------|----------------------|----------------------|
| | 03 | | 04 | | 09 | | 17 | | 19 | | 22 | | 24 | | | | |
| | t_{rel} | r_{rel} | t_{rel} | r_{rel} | t_{rel} | r_{rel} | t_{rel} | r_{rel} | t_{rel} | r_{rel} | t_{rel} | r_{rel} | t_{rel} | r_{rel} | t_{rel} | r_{rel} | |
| Classical-based methods | ICP-po2po | 0.39 | 1.00 | 0.21 | 1.14 | 0.15 | 0.72 | 0.16 | 0.53 | 1.40 | 4.70 | 0.44 | 0.76 | 0.24 | 0.77 | 0.427 | 1.374 |
| | ICP-po2pl | 0.42 | 2.19 | 0.37 | 1.83 | 0.50 | 1.32 | 0.23 | 0.68 | 3.04 | 5.62 | 0.42 | 1.20 | 0.35 | 0.67 | 0.761 | 1.930 |
| | GICP | 0.46 | 0.68 | 0.30 | 0.39 | 0.51 | 0.32 | 0.40 | 0.10 | 0.51 | 1.23 | 0.34 | 0.57 | 0.15 | 0.30 | 0.381 | 0.513 |
| | NDT | 0.55 | 1.60 | 0.47 | 0.91 | 0.46 | 0.56 | 0.44 | 0.40 | 1.33 | 2.58 | 0.47 | 1.10 | 0.36 | 1.84 | 0.583 | 1.284 |
| LiDAR-based methods | Full A-LOAM | NA | NA | 0.03 | 0.09 | 0.04 | 0.19 | 0.02 | 0.04 | 0.38 | 1.35 | 0.06 | 0.18 | 0.06 | 0.20 | 0.098 | 0.342 |
| | A-LOAM w/o mapping | NA | NA | 0.14 | 0.35 | 0.16 | 1.23 | 0.09 | 0.26 | 1.17 | 4.63 | 0.27 | 0.92 | 0.16 | 0.81 | 0.332 | 1.370 |
| | PWCLO-Net | 0.26 | 0.37 | 0.31 | 0.40 | 0.38 | 0.55 | 0.27 | 0.39 | 1.23 | 0.91 | 0.23 | 0.35 | 0.46 | 0.82 | 0.449 | 0.541 |
| 4D Radar-based methods | RaFlow | 0.87 | 2.09 | 0.07 | 0.44 | 0.11 | 0.09 | 0.13 | 0.03 | 1.22 | 4.09 | 0.72 | 1.34 | 0.25 | 1.14 | 0.481 | 1.317 |
| | CMFlow | 0.06 | 0.10 | 0.05 | 0.09 | 0.09 | 0.14 | 0.06 | 0.03 | 0.28 | 0.94 | 0.14 | 0.29 | 0.12 | 0.58 | 0.114 | 0.310 |
| | 4DRONet | 0.08 | 0.10 | 0.04 | 0.07 | 0.13 | 0.38 | 0.09 | 0.10 | 0.91 | 0.62 | 0.23 | 0.32 | 0.28 | 1.20 | 0.251 | 0.398 |
| | CAO-RONet | 0.049 | 0.034 | 0.042 | 0.040 | 0.064 | 0.089 | 0.082 | 0.063 | 0.135 | 0.076 | 0.102 | 0.013 | 0.024 | 0.045 | 0.071 | 0.051 |
| Ours | | 0.021 | 0.018 | 0.022 | 0.026 | 0.017 | 0.016 | 0.018 | 0.021 | 0.021 | 0.038 | 0.025 | 0.024 | 0.034 | 0.048 | 0.023 67.6% | 0.027 47.1% |

Table 1: The 4D radar odometry experiment results on the VoD dataset [25]. t_{rel} and r_{rel} denote the average translational RMSE (m/m) and rotational RMSE ($^{\circ}$ /m), respectively, on all possible subsequences in the length of 20, 40, ..., 160m. All methods listed use 4D radar point clouds as input. Full A-LOAM is a complete SLAM system and others only include odometry.

4.2 Supervision

We supervise our network using a pose loss. Given a set of ground truth poses $\{\tilde{\mathbf{T}}\}_{i=1}^L$ and predicted poses $\{\mathbf{T}\}_{i=1}^L$, the pose loss is taken to be the distance between the ground truth and predicted poses:

$$L_{pose} = \sum_{i=1}^L \left\| \text{Log}_{SE3} \left((\tilde{\mathbf{T}}^i)^{-1} \cdot \mathbf{T}^i \right) \right\|^2, \quad (13)$$

where $\text{Log}_{SE3}(\cdot)$ represents the logarithmic map from Lie group to Lie algebra.

4.3 Training Details

We train for 30 epochs on an A100 GPU with a batch size of 4. We use the Adam optimizer and start with an initial learning rate of $2e^{-4}$, which decays by a factor of 0.1 every 10 epochs. N is set to be 512 in the proposed network. The radar point heights are constrained within the range of $[-2m, 10m]$ to retain reliable points. During training, random transformation matrices are applied to the points and the ground truth pose to increase data diversity. We select 8 cluster centers. The iteration operator is unrolled for 15 iterations during training, with two bundle adjustment steps performed within each iteration. The ground truth pose of the first frame in each training sequence serves as the initial pose for all radar frames in that sequence, with the initial point motion flow set to zero.

4.4 4DRO System

We apply the backbone network during inference to construct a fully 4DRO system that processes a 4D radar point cloud stream for real-time localization.

Initialization: We initialize with 8 frames, continuously adding new frames until 8 frames are accumulated, after which we perform 12 iterations of the iteration operator.

Tracking: We maintain a frame graph. After initialization, when a new frame is added, we extract features and add the new frame to the frame graph, establishing edges with all frames within an index distance of 2. The pose is initialized using a linear motion model. We then run four iterations of the iteration operator, performing two bundle adjustment iterations within each iteration. We fix the initial frame’s pose in the frame graph to remove gauge freedom. After the new frame is tracked, we remove the oldest frame.

5 Experiments

We evaluate the method on two 4D radar odometry benchmarks, with dataset details in the appendix. We follow protocols of DVLO [45] to evaluate our method with two metrics: (1) Average sequence translational RMSE (%). (2) Average sequence rotational RMSE ($^{\circ}/100m$).

5.1 Performance Evaluation

VoD Results: Quantitative results are listed in Table 1. ICP-point2point (ICP-po2po) [27], ICP-

| Method | Input | Mean | | | | | | | | | |
|--------------------|-------|-------------|--------------|-------------|-------------|--------------|--------------|--------------|-------------|--------------|---------------------|
| | | t_{rel} | r_{rel} | t_{rel} | r_{rel} | t_{rel} | r_{rel} | t_{rel} | r_{rel} | t_{rel} | r_{rel} |
| Full A-LOAM | L | 0.05 | 0.11 | 0.03 | 0.10 | 0.03 | 0.08 | 0.02 | 0.02 | 0.05 | 0.14 |
| A-LOAM w/o mapping | L | 0.06 | 0.10 | 0.03 | 0.12 | 0.06 | 0.06 | 0.03 | 0.02 | 0.14 | 0.19 |
| 4DRVONet | C+R | 0.02 | 0.02 | 0.01 | 0.02 | 0.03 | 0.05 | 0.11 | 0.03 | 0.26 | 0.08 |
| Ours | R | 0.021 | 0.018 | 0.022 | 0.026 | 0.017 | 0.016 | 0.018 | 0.021 | 0.038 | 0.025 |
| | | | | | | | | | | 0.024 | 0.034 |
| | | | | | | | | | | 0.048 | 0.023, 32.4% |
| | | | | | | | | | | | 0.027, 59.7% |

Table 2: The experiment results on the VoD dataset [25] using methods with LiDAR or 4D radar-camera inputs. ‘L’, ‘C’, and ‘R’ represent LiDAR, camera, and 4D radar, respectively.

| Method | Input | Mean | | | | | | | |
|--------------------|-------|-------------|-------------|-------------|-------------|-----------|-----------|--------------|--------------|
| | | if | iaf | st | t_{rel} | r_{rel} | t_{rel} | | |
| Full A-LOAM | L | 0.92 | 0.41 | 1.54 | 0.54 | 1.93 | 2.54 | 1.465 | 1.163 |
| A-LOAM w/o mapping | L | 14.74 | 4.10 | 14.75 | 3.88 | 12.26 | 9.62 | 13.916 | 5.867 |
| ICP-po2po | R | 35.54 | 13.98 | 37.09 | 10.18 | 26.31 | 60.07 | 32.980 | 28.077 |
| ICP-po2pl | R | 27.16 | 11.17 | 30.81 | 11.35 | 20.70 | 39.96 | 26.226 | 20.827 |
| GICP | R | 31.20 | 11.37 | 31.79 | 9.7 | 26.36 | 51.22 | 29.785 | 24.097 |
| 4DRadarSLAM | R | 13.32 | 6.11 | 16.13 | 6.62 | 10.70 | 15.43 | 13.386 | 9.387 |
| Ours | R | 3.92 | 1.85 | 6.10 | 2.21 | 3.76 | 3.94 | 4.598 | 2.670 |

Table 3: The experiment results on the Snail-Radar dataset [26]. t_{rel} and r_{rel} denote the average translational RMSE (%) and rotational RMSE ($^{\circ}/100m$), respectively, on all possible subsequences in the length of 100, 200, ..., 800m. ‘L’ and ‘R’ represent LiDAR and 4D radar, respectively.

point2plane (ICP-po2pl) [28], GICP [29], NDT [31] are several classical point cloud odometry methods. PWCLO-Net [6] is currently the leading open-source deep learning-based LiDAR odometry method that directly processes raw 3D point clouds. A-LOAM [46] is a conventional LiDAR odometry method that achieves state-of-the-art performance on the KITTI Odometry benchmark [47]. We use 4D radar point clouds as input for these methods. The experimental results indicate that, while these methods perform effectively on LiDAR point clouds, their performance deteriorates significantly on 4D radar point clouds due to the sparse, noisy, and non-panoramic characteristics of 4D radar data. RaFlow [48] and CMFlow [34] are 4D radar-based scene flow estimation networks incorporating odometry estimation as an intermediate task. 4DRONet [23] and CAO-RONet [24] are odometry networks specifically tailored for processing 4D radar data. Our method outperforms all previous 4D radar odometry methods due to its innovative architecture and robust point cloud feature extraction. Notably, our method reduces mean translation and rotation errors by 67.6% and 47.1%, respectively, compared to the previous best learning-based method.

Table 2 shows the evaluation results of Full A-LOAM and A-LOAM without mapping using 64-beam LiDAR point clouds as input, along with the results of the 4D radar-camera fusion odometry method (4DRVONet) [22]. It can be seen that our method achieves competitive performance with Full A-LOAM in short-range localization. Compared with 4DRVONet, our method achieves a reduction of 72.3% in mean translation error and 59.7% in mean rotation error on the test sequences. The experiment results prove the effectiveness of our proposed neural-optimization iteration module and demonstrate its great potential in 4D radar odometry tasks.

Snail-Radar Results: Compared with the VoD dataset [25], the Snail-Radar Dataset [26] contains longer trajectories and more complex environments, posing greater challenges to odometry stability. We compare our method with ICP-based point cloud odometry methods and 4DRadarSLAM [19], a classical 4D radar SLAM method. We turn off the loop closure detection in 4DRadarSLAM to ensure a fair comparison. Additionally, we present the results of Full A-LOAM and A-LOAM without mapping, using 32-beam LiDAR point clouds as input. Table 3 indicates that, while our method is slightly less effective than Full A-LOAM in long-range odometry localization, it narrows the performance gap with leading LiDAR odometry methods and significantly outperforms A-LOAM without mapping. Furthermore, compared with 4DRadarSLAM, our method reduces mean translation and rotation errors by 65.7% and 71.6%, respectively.

5.2 Ablation Study

We perform ablation experiments on the Snail-Radar Dataset to evaluate the effectiveness of each module in DNOI-4DRO. The training/testing details are the same as in Sec. 4.

Feature Extraction: We evaluate the effectiveness of each component in the proposed feature extraction network. As shown in Table 4(a), removing any individual module leads to a noticeable drop in pose estimation accuracy, highlighting each module’s critical role in capturing fine-grained 4D radar features and enhancing the overall 4DRO performance.

| Method | 03 | | 04 | | 09 | | 17 | | 19 | | 22 | | 24 | | Mean | |
|--|--------------|--------------|--------------|--------------|--------------|--------------|--------------|--------------|--------------|--------------|--------------|--------------|--------------|--------------|--------------|--------------|
| | t_{rel} | r_{rel} |
| (a) Ours w/o multi-scale geometric feature | 0.049 | 0.067 | 0.026 | 0.033 | 0.030 | 0.012 | 0.017 | 0.023 | 0.033 | 0.150 | 0.030 | 0.049 | 0.033 | 0.033 | 0.030 | 0.052 |
| | 0.043 | 0.072 | 0.025 | 0.030 | 0.019 | 0.012 | 0.017 | 0.021 | 0.050 | 0.053 | 0.023 | 0.038 | 0.031 | 0.030 | 0.030 | 0.037 |
| | 0.032 | 0.037 | 0.027 | 0.031 | 0.016 | 0.014 | 0.018 | 0.021 | 0.045 | 0.071 | 0.027 | 0.039 | 0.027 | 0.026 | 0.027 | 0.034 |
| (b) Ours w/o AMBA layer | 0.053 | 0.115 | 0.024 | 0.085 | 0.020 | 0.053 | 0.020 | 0.048 | 0.021 | 0.159 | 0.037 | 0.076 | 0.033 | 0.089 | 0.030 | 0.089 |
| | 0.470 | 0.814 | 0.338 | 0.701 | 0.455 | 0.704 | 0.390 | 0.442 | 0.133 | 0.021 | 0.389 | 0.600 | 0.259 | 0.873 | 0.348 | 0.594 |
| | 0.035 | 0.056 | 0.021 | 0.031 | 0.016 | 0.018 | 0.015 | 0.015 | 0.039 | 0.021 | 0.016 | 0.028 | 0.027 | 0.034 | 0.024 | 0.029 |
| (c) Ours w/o confidence weight | 0.039 | 0.041 | 0.027 | 0.040 | 0.033 | 0.027 | 0.032 | 0.025 | 0.189 | 0.259 | 0.048 | 0.043 | 0.049 | 0.109 | 0.060 | 0.078 |
| | 0.056 | 0.092 | 0.031 | 0.039 | 0.032 | 0.049 | 0.097 | 0.015 | 0.065 | 0.075 | 0.024 | 0.037 | 0.037 | 0.041 | 0.049 | 0.050 |
| | 0.035 | 0.056 | 0.021 | 0.031 | 0.016 | 0.018 | 0.015 | 0.015 | 0.039 | 0.021 | 0.016 | 0.028 | 0.027 | 0.034 | 0.024 | 0.029 |

Table 4: The ablation study results of 4D Radar odometry on the VoD dataset [25].

— Ground Truth — 4DRONet — A-LOAM w/o mapping(LiDAR Input) — Full A-LOAM (LiDAR Input) ● Start Point
— Ours — PWCLO-Net — 4DRVNet

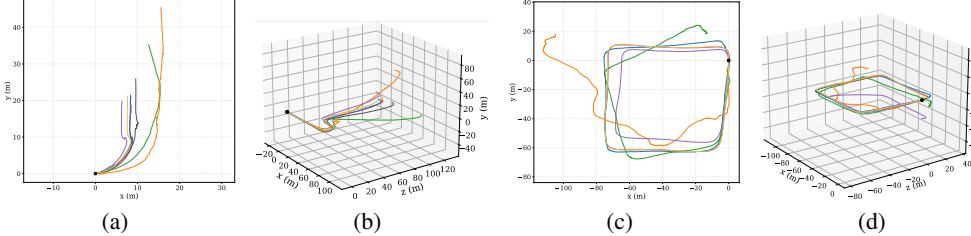


Figure 4: 3D and 2D trajectory results for VoD test sequences 19 (a) and 22 (b), and Snail-Radar test sequences st (c) and (d). Our method obtains the most accurate trajectory.

Iteration Operator: We remove the AMBA layer during training, relying on point motion flow supervision to train the network. Then, we eliminate the entire iteration operator and directly regress poses from correlation features, which means that completely discarding the geometric optimization process. As shown in Table 4(b), removing either component significantly reduces pose estimation accuracy. These results highlight the crucial role of the introduced geometric optimization mechanism in enhancing estimation precision.

Confidence Weight: First, we remove the confidence weight by setting all weights to 1. Then, we calculate a confidence value for each point, assuming that the point has equal importance in pose estimation across different directions. Table 4(c) show that the proposed confidence weight and fine-grained estimation across different directions contribute to better results.

5.3 Visualization

We visualize 3D and 2D trajectories based on our estimated pose on the VoD and Snail-Radar datasets, as shown in Fig. 4. These figures show that our odometry can track the trajectory of the ground truth fairly well. Although we do not have the mapping procedure, our odometry achieves trajectory accuracy comparable to that of Full A-LOAM in short-range localization. Furthermore, our approach significantly reduces odometry drift along the Z-axis compared to other methods. Fig. 5 illustrates the clustering results. The clustering-based method effectively mitigates the constraints of the receptive field, facilitating extracting features that belong to the same category (e.g., vehicles, curbs, walls). This approach enables point features to exhibit class awareness, improving their representational capacity.

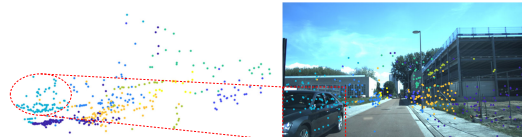


Figure 5: The Visualization of clustering results. The clustering-based method effectively mitigates the constraints of the receptive field, facilitating extracting features that belong to the same category (e.g., vehicles, curbs, walls). This approach enables point features to exhibit class awareness, improving their representational capacity.

6 Conclusion and Limitation

We introduce DNOI-4DRO, an end-to-end neural architecture for 4D radar odometry, which combines the strengths of both classical approaches and deep networks through a differentiable neural-optimization iteration module. We compare against existing approaches and show strong performance across several datasets. The current research primarily focuses on optimization techniques based on sliding windows. Effective global optimization can significantly enhance pose estimation accuracy.

Future efforts will be directed toward exploring more efficient strategies for keyframe selection and the development of global optimization frameworks.

References

- [1] Zachary Teed and Jia Deng. Droid-slam: Deep visual slam for monocular, stereo, and rgb-d cameras. *Advances in neural information processing systems*, 34:16558–16569, 2021.
- [2] Zachary Teed, Lahav Lipson, and Jia Deng. Deep patch visual odometry. *Advances in Neural Information Processing Systems*, 36:39033–39051, 2023.
- [3] Lahav Lipson and Jia Deng. Multi-session slam with differentiable wide-baseline pose optimization. In *Proceedings of the IEEE/CVF Conference on Computer Vision and Pattern Recognition*, pages 19626–19635, 2024.
- [4] Shuo Wang, Wanting Li, Yongcai Wang, Zhaoxin Fan, Zhe Huang, Xudong Cai, Jian Zhao, and Deying Li. Mambavo: Deep visual odometry based on sequential matching refinement and training smoothing. *arXiv preprint arXiv:2412.20082*, 2024.
- [5] Weirong Chen, Le Chen, Rui Wang, and Marc Pollefeys. Leap-vo: Long-term effective any point tracking for visual odometry. In *Proceedings of the IEEE/CVF Conference on Computer Vision and Pattern Recognition*, pages 19844–19853, 2024.
- [6] Guangming Wang, Xinrui Wu, Zhe Liu, and Hesheng Wang. Pwclo-net: Deep lidar odometry in 3d point clouds using hierarchical embedding mask optimization. In *Proceedings of the IEEE/CVF conference on computer vision and pattern recognition*, pages 15910–15919, 2021.
- [7] Qing Li, Shaoyang Chen, Cheng Wang, Xin Li, Chenglu Wen, Ming Cheng, and Jonathan Li. Lo-net: Deep real-time lidar odometry. In *Proceedings of the IEEE/CVF conference on computer vision and pattern recognition*, pages 8473–8482, 2019.
- [8] Guangming Wang, Xinrui Wu, Shuyang Jiang, Zhe Liu, and Hesheng Wang. Efficient 3d deep lidar odometry. *IEEE Transactions on Pattern Analysis and Machine Intelligence*, 45(5):5749–5765, 2022.
- [9] Jiuming Liu, Guangming Wang, Chaokang Jiang, Zhe Liu, and Hesheng Wang. Translo: A window-based masked point transformer framework for large-scale lidar odometry. In *Proceedings of the AAAI Conference on Artificial Intelligence*, volume 37, pages 1683–1691, 2023.
- [10] Sk Aziz Ali, Djamila Aouada, Gerd Reis, and Didier Stricker. Delo: deep evidential lidar odometry using partial optimal transport. In *Proceedings of the IEEE/CVF International Conference on Computer Vision*, pages 4517–4526, 2023.
- [11] Junyuan Deng, Qi Wu, Xieyuanli Chen, Songpengcheng Xia, Zhen Sun, Guoqing Liu, Wenxian Yu, and Ling Pei. Nerf-loam: Neural implicit representation for large-scale incremental lidar odometry and mapping. In *Proceedings of the IEEE/CVF International Conference on Computer Vision*, pages 8218–8227, 2023.
- [12] Huixin Zhang, Guangming Wang, Xinrui Wu, Chenfeng Xu, Mingyu Ding, Masayoshi Tomizuka, Wei Zhan, and Hesheng Wang. Dslo: Deep sequence lidar odometry based on inconsistent spatio-temporal propagation. In *2024 IEEE/RSJ International Conference on Intelligent Robots and Systems (IROS)*, pages 10672–10677. IEEE, 2024.
- [13] Zhijun Pan, Fangqiang Ding, Hantao Zhong, and Chris Xiaoxuan Lu. Rattrack: moving object detection and tracking with 4d radar point cloud. In *2024 IEEE International Conference on Robotics and Automation (ICRA)*, pages 4480–4487. IEEE, 2024.
- [14] Fangqiang Ding, Zhen Luo, Peijun Zhao, and Chris Xiaoxuan Lu. milliflow: Scene flow estimation on mmwave radar point cloud for human motion sensing. In *European Conference on Computer Vision*, pages 202–221. Springer, 2024.

[15] Fangqiang Ding, Xiangyu Wen, Yunzhou Zhu, Yiming Li, and Chris Xiao-xuan Lu. Radarocc: Robust 3d occupancy prediction with 4d imaging radar. *Advances in Neural Information Processing Systems*, 37:101589–101617, 2024.

[16] Zhiwei Lin, Zhe Liu, Zhongyu Xia, Xinhao Wang, Yongtao Wang, Shengxiang Qi, Yang Dong, Nan Dong, Le Zhang, and Ce Zhu. Rcbevdet: radar-camera fusion in bird’s eye view for 3d object detection. In *Proceedings of the IEEE/CVF Conference on Computer Vision and Pattern Recognition*, pages 14928–14937, 2024.

[17] Guohao Peng, Heshan Li, Yangyang Zhao, Jun Zhang, Zhenyu Wu, Pengyu Zheng, and Danwei Wang. Transloc4d: Transformer-based 4d radar place recognition. In *Proceedings of the IEEE/CVF Conference on Computer Vision and Pattern Recognition*, pages 17595–17605, 2024.

[18] Runwei Guan, Ruixiao Zhang, Ningwei Ouyang, Jianan Liu, Ka Lok Man, Xiaohao Cai, Ming Xu, Jeremy Smith, Eng Gee Lim, Yutao Yue, et al. Talk2radar: Bridging natural language with 4d mmwave radar for 3d referring expression comprehension. *arXiv preprint arXiv:2405.12821*, 2024.

[19] Jun Zhang, Huayang Zhuge, Zhenyu Wu, Guohao Peng, Mingxing Wen, Yiyao Liu, and Danwei Wang. 4dradar slam: A 4d imaging radar slam system for large-scale environments based on pose graph optimization. In *2023 IEEE International Conference on Robotics and Automation (ICRA)*, pages 8333–8340. IEEE, 2023.

[20] Xingyi Li, Han Zhang, and Weidong Chen. 4d radar-based pose graph slam with ego-velocity pre-integration factor. *IEEE Robotics and Automation Letters*, 8(8):5124–5131, 2023.

[21] Xiaoyi Wu, Yushuai Chen, Zhan Li, Ziyang Hong, and Liang Hu. Efear-4d: Ego-velocity filtering for efficient and accurate 4d radar odometry. *IEEE Robotics and Automation Letters*, 2024.

[22] Guirong Zhuo, Shouyi Lu, Huanyu Zhou, Lianqing Zheng, Mingyu Zhou, and Lu Xiong. 4drvo-net: Deep 4d radar–visual odometry using multi-modal and multi-scale adaptive fusion. *IEEE Transactions on Intelligent Vehicles*, 9(6):5065–5079, 2024.

[23] Shouyi Lu, Guirong Zhuo, Lu Xiong, Xichan Zhu, Lianqing Zheng, Zihang He, Mingyu Zhou, Xinfai Lu, and Jie Bai. Efficient deep-learning 4d automotive radar odometry method. *IEEE Transactions on Intelligent Vehicles*, 9(1):879–892, 2024.

[24] Zhiheng Li, Yubo Cui, Ningyuan Huang, Chenglin Pang, and Zheng Fang. Cao-ronet: A robust 4d radar odometry with exploring more information from low-quality points. *arXiv preprint arXiv:2503.01438*, 2025.

[25] Andras Palfy, Ewoud Pool, Srimannarayana Baratam, Julian FP Kooij, and Dariu M Gavrila. Multi-class road user detection with 3+ 1d radar in the view-of-delft dataset. *IEEE Robotics and Automation Letters*, 7(2):4961–4968, 2022.

[26] Jianzhu Huai, Binliang Wang, Yuan Zhuang, Yiwen Chen, Qipeng Li, and Yulong Han. Snail radar: A large-scale diverse benchmark for evaluating 4d-radar-based slam. *arXiv preprint arXiv:2407.11705*, 2024.

[27] Paul J Besl and Neil D McKay. Method for registration of 3-d shapes. In *Sensor fusion IV: control paradigms and data structures*, volume 1611, pages 586–606. Spie, 1992.

[28] Yang Chen and Gérard Medioni. Object modelling by registration of multiple range images. *Image and vision computing*, 10(3):145–155, 1992.

[29] Aleksandr Segal, Dirk Haehnel, and Sebastian Thrun. Generalized-icp. In *Robotics: science and systems*, volume 2, page 435. Seattle, WA, 2009.

[30] Dong Wang, Stefan May, and Andreas Nuechter. Riv-slam: Radar-inertial-velocity optimization based graph slam. In *2024 IEEE 20th International Conference on Automation Science and Engineering (CASE)*, pages 774–781. IEEE, 2024.

[31] Todor Stoyanov, Martin Magnusson, Henrik Andreasson, and Achim J Lilienthal. Fast and accurate scan registration through minimization of the distance between compact 3d ndt representations. *The International Journal of Robotics Research*, 31(12):1377–1393, 2012.

[32] Yuan Zhuang, Binliang Wang, Jianzhu Huai, and Miao Li. 4d iriom: 4d imaging radar inertial odometry and mapping. *IEEE Robotics and Automation Letters*, 8(6):3246–3253, 2023.

[33] Huanyu Zhou, Shouyi Lu, and Guirong Zhuo. Self-supervised 4-d radar odometry for autonomous vehicles. In *2023 IEEE 26th International Conference on Intelligent Transportation Systems (ITSC)*, pages 764–769, 2023.

[34] Fangqiang Ding, Andras Palfy, Dariu M Gavrila, and Chris Xiaoxuan Lu. Hidden gems: 4d radar scene flow learning using cross-modal supervision. In *Proceedings of the IEEE/CVF Conference on Computer Vision and Pattern Recognition*, pages 9340–9349, 2023.

[35] Zachary Teed and Jia Deng. Raft-3d: Scene flow using rigid-motion embeddings. In *Proceedings of the IEEE/CVF conference on computer vision and pattern recognition*, pages 8375–8384, 2021.

[36] Zachary Teed and Jia Deng. Raft: Recurrent all-pairs field transforms for optical flow. In *Computer Vision–ECCV 2020: 16th European Conference, Glasgow, UK, August 23–28, 2020, Proceedings, Part II 16*, pages 402–419. Springer, 2020.

[37] Kyunghyun Cho. On the properties of neural machine translation: Encoder-decoder approaches. *arXiv preprint arXiv:1409.1259*, 2014.

[38] Charles Ruizhongtai Qi, Li Yi, Hao Su, and Leonidas J Guibas. Pointnet++: Deep hierarchical feature learning on point sets in a metric space. *Advances in neural information processing systems*, 30, 2017.

[39] Xu Ma, Yuqian Zhou, Huan Wang, Can Qin, Bin Sun, Chang Liu, and Yun Fu. Image as set of points. *arXiv preprint arXiv:2303.01494*, 2023.

[40] Charles R Qi, Hao Su, Kaichun Mo, and Leonidas J Guibas. Pointnet: Deep learning on point sets for 3d classification and segmentation. In *Proceedings of the IEEE conference on computer vision and pattern recognition*, pages 652–660, 2017.

[41] Ashish Vaswani, Noam Shazeer, Niki Parmar, Jakob Uszkoreit, Llion Jones, Aidan N Gomez, Łukasz Kaiser, and Illia Polosukhin. Attention is all you need. *Advances in neural information processing systems*, 30, 2017.

[42] Guangming Wang, Xinrui Wu, Zhe Liu, and Hesheng Wang. Hierarchical attention learning of scene flow in 3d point clouds. *IEEE Transactions on Image Processing*, 30:5168–5181, 2021.

[43] Yi Wei, Ziyi Wang, Yongming Rao, Jiwen Lu, and Jie Zhou. Pv-raft: Point-voxel correlation fields for scene flow estimation of point clouds. In *Proceedings of the IEEE/CVF conference on computer vision and pattern recognition*, pages 6954–6963, 2021.

[44] Zachary Teed and Jia Deng. Tangent space backpropagation for 3d transformation groups. In *Proceedings of the IEEE/CVF conference on computer vision and pattern recognition*, pages 10338–10347, 2021.

[45] Jiuming Liu, Dong Zhuo, Zhiheng Feng, Siting Zhu, Chensheng Peng, Zhe Liu, and Hesheng Wang. Dvlo: Deep visual-lidar odometry with local-to-global feature fusion and bi-directional structure alignment. In *European Conference on Computer Vision*, pages 475–493. Springer, 2024.

[46] Ji Zhang and Sanjiv Singh. Low-drift and real-time lidar odometry and mapping. *Autonomous robots*, 41:401–416, 2017.

[47] Andreas Geiger, Philip Lenz, Christoph Stiller, and Raquel Urtasun. Vision meets robotics: The kitti dataset. *The international journal of robotics research*, 32(11):1231–1237, 2013.

[48] Fangqiang Ding, Zhijun Pan, Yimin Deng, Jianning Deng, and Chris Xiaoxuan Lu. Self-supervised scene flow estimation with 4-d automotive radar. *IEEE Robotics and Automation Letters*, 7(3):8233–8240, 2022.

A Technical Appendices and Supplementary Material

A.1 Overview

This supplementary material provides more detailed implementation specifics in Sec. A.2. Sec. A.3 presents experimental results regarding runtime. Sec. A.4 shows additional qualitative evaluation results. Sec. A.5 discusses the broader impacts of the algorithm introduced in this paper.

A.2 Detailed Implementation Specifics

A.2.1 Data Augmentation Parameters

We adopt the data augmentation method from [6]. Specifically, we expand the training dataset by generating augmentation matrix \mathbf{T}^{aug} through rotation matrix \mathbf{R}^{aug} and translation vector \mathbf{t}^{aug} . Varied values of the yaw-pitch-roll Euler angles are generated by Gaussian distribution around 0° . We set the standard deviations of the yaw, pitch, and roll Euler angles to 0.05° , 0.01° , and 0.01° , respectively. We set the standard deviations for the translation in the XYZ directions to $0.2m$, $1.0m$, and $0.05m$, respectively. In these Gaussian distributions, we select the data in the range of 2 times standard deviation around the mean value for data augmentation.

The composed \mathbf{T}^{aug} from \mathbf{R}^{aug} and \mathbf{t}^{aug} is then used to augment the \mathbf{PC}^2 to obtain new point clouds $\mathbf{PC}^{2,\text{aug}}$.

A.2.2 The Detailed Introduction of the Dataset

View-of-Delft Automotive Dataset (VoD) [25] is collected from the Delft campus, suburbs, and old town, integrating data from various sensors, including 4D radar. The dataset comprises 8682 frames, organized into 24 sequences based on frame continuity. We adopt the predefined sets from CMFlow [34] to evaluate the network’s performance for training, validation, and testing purposes.

Snail-Radar Dataset [26] is designed explicitly for 4D radar-based localization and mapping, covering campus and highway scenes under varied weather and lighting conditions. The dataset comprises 44 sequences collected across eight distinct scenes. One sequence is selected from each scene to avoid trajectory redundancy, resulting in eight sequences. Among these, five sequences (52,540 frames) are allocated for model training, while the remaining three sequences (23,037 frames) are designated for testing. The sequence lengths and weather and lighting conditions during data collection are presented in Table 5. As shown in Fig. 6, all test sequences were collected on rainy nights, where adverse weather conditions significantly impacted odometry stability. However, despite the challenging weather conditions, the method proposed in this paper still achieves high accuracy (Table 3), further confirming the approach’s effectiveness and the potential of 4D radar for application in complex environments.

| Scene | Sequence | Split | Dist.(m)/Dur.(sec) | Weather/Lighting |
|-------|----------------|-------|--------------------|-------------------|
| bc | 20231105/6 | train | 251/144 | moderate, rain |
| sl | 20231019/1 | train | 1919/460 | night |
| ss | 20231105/4 | train | 895/395 | heavy rain |
| iaef | 20240115/2 | train | 6641/1374 | |
| 81r | 20240116 eve/3 | train | 8521/1293 | night |
| if | 20231213/4 | test | 2227/494 | light rain, night |
| iaf | 20231213/2 | test | 4603/938 | light rain, night |
| st | 20231213/1 | test | 276/126 | light rain, night |

Table 5: Description of Snail-Radar Dataset [26].

A.3 Runtime Analysis

Efficiency is another highly significant factor in real-time SLAM systems. We evaluate the runtime of each module in DNOI-4DRO on the VoD dataset, as shown in Table 6. Since the 4D radar points in the VoD dataset are captured at a 10Hz frequency, our method has only 43.2ms inference time, which has the potential for real-time application.



Figure 6: Examples of three test sequences from the Snail-Radar dataset [26], all captured in nighttime rainy conditions.

| Module | Feature Extraction | Update Operator | Total |
|-------------|--------------------|-----------------|-------|
| Runtime(ms) | 6.8 | 36.4 | 43.2 |

Table 6: Average inference time of different modules on the test sequence of the VoD dataset[25].

A.4 Additional Qualitative Results

A.4.1 Confidence Weight Visualization

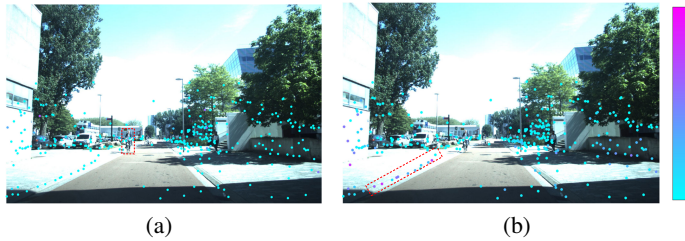


Figure 7: Confidence weight visualization. (a) Confidence in the X direction. (b) Confidence in the Y direction.

Fig. 7 shows the confidence weights estimated by the network on the VoD dataset [25]. The figure demonstrates that the network assigns varying confidence weights to the same point across different directions. In the X direction, high-confidence points are primarily selected from the vertical plane at intermediate distances, as these points provide stable longitudinal constraints. For the Y direction, high-confidence points are concentrated on those located along the road edge and the left-right planes, which offer reliable lateral constraints. Additionally, points on dynamic objects, such as cyclists, are assigned low confidence, thereby minimizing their adverse impact on the odometry estimation.

A.4.2 Average Translation and Rotation Errors

Fig. 8(a) shows the average translation and rotation error on VoD test sequences. Our method performs better in translation and rotation errors across various path lengths. Notably, our method exhibits a clear advantage compared to other odometry methods that use 4D radar point clouds as input. Additionally, our method yields superior results in most path lengths compared to A-LOAM [46] with mapping optimization, which uses LiDAR point clouds as input.

Fig. 8(b) presents the average translation and rotation error on the Snail-Radar test sequences. The longer trajectories on the Snail-Radar dataset allow the mapping optimization in Full A-LOAM to demonstrate its advantages fully. Although our method slightly underperforms compared to Full A-LOAM, which utilizes 32-beam LiDAR point clouds as input, it substantially narrows the performance gap with Full A-LOAM compared to other methods. Furthermore, considering that the number of 4D radar points is approximately 1% of the 32-beam LiDAR point clouds and that our method does not include a mapping optimization process, we believe the performance gap with Full A-LOAM is within an acceptable range, with potential for further enhancement.

A.4.3 More Trajectory Results on VoD Dataset

We list all visualized trajectory results on test sequences of VoD dataset [25] with the ground truth in Fig. 9, excluding the results in our submitted paper. The results demonstrate that our method

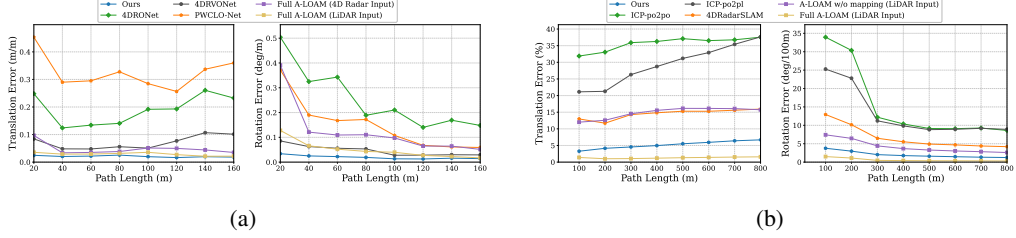


Figure 8: (a) Average translational and rotational error on VoD test sequences on all possible subsequences in the length of 20, 40, ..., 160m. (b) Average translational and rotational error on Snail-Radar test sequences on all possible subsequences in the length of 100, 200, ..., 800m.

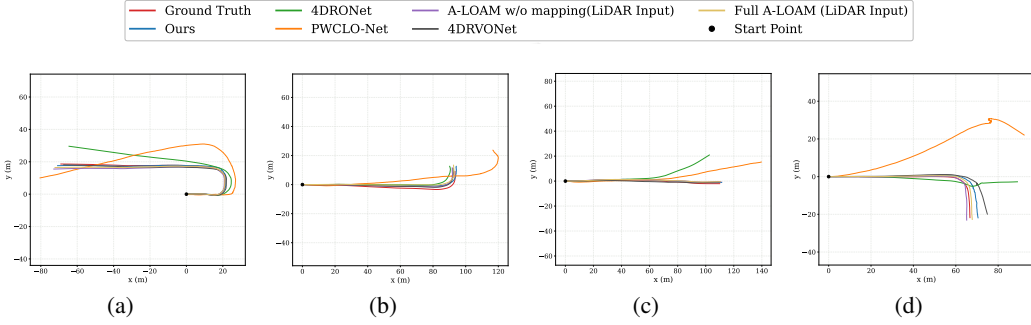


Figure 9: 2D trajectory results on VoD test sequences with ground truth. Our method achieves trajectory accuracy comparable to that of Full A-LOAM. (a) 2D Trajectory Plots of Seq. 03. (b) 2D Trajectory Plots of Seq. 04. (c) 2D Trajectory Plots of Seq. 09. (c) 2D Trajectory Plots of Seq. 24.

outperforms existing 4D radar odometry methods and the A-LOAM without mapping using 64-beam LiDAR point clouds across all test sequences. Furthermore, it exceeds the performance of both the 4D radar-camera fusion odometry method and the Full A-LOAM using 64-beam LiDAR point clouds in most sequences.

A.4.4 Reconstruction

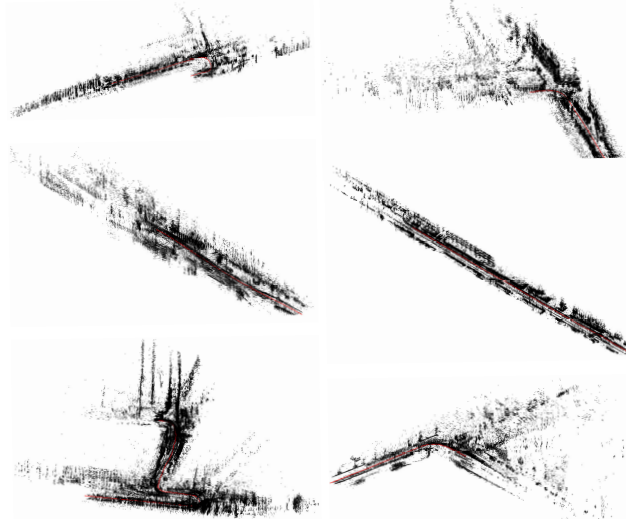


Figure 10: Example reconstruction on VoD dataset [25].

A.5 Broader Impacts

4D millimeter-wave radar is a low-cost, all-weather sensor. The 4D radar-based odometry method proposed in this paper enables high-precision localization for autonomous driving and robotics across diverse environments, particularly in challenging weather conditions. Moreover, the method demonstrates strong potential for real-time applications, facilitating its deployment in practical scenarios. By offering an efficient and robust solution, it strongly supports technological advancements in autonomous driving and robotics.